

# Materials Horizons

Accepted Manuscript

This article can be cited before page numbers have been issued, to do this please use: K. Jiang, Y. Jiang, Z. Liang, W. Zhang, H. Liu, J. Shi, S. Wang, Z. Zhong and Y. Du, *Mater. Horiz.*, 2025, DOI: 10.1039/D5MH01041A.



This is an Accepted Manuscript, which has been through the Royal Society of Chemistry peer review process and has been accepted for publication.

Accepted Manuscripts are published online shortly after acceptance, before technical editing, formatting and proof reading. Using this free service, authors can make their results available to the community, in citable form, before we publish the edited article. We will replace this Accepted Manuscript with the edited and formatted Advance Article as soon as it is available.

You can find more information about Accepted Manuscripts in the [Information for Authors](#).

Please note that technical editing may introduce minor changes to the text and/or graphics, which may alter content. The journal's standard [Terms & Conditions](#) and the [Ethical guidelines](#) still apply. In no event shall the Royal Society of Chemistry be held responsible for any errors or omissions in this Accepted Manuscript or any consequences arising from the use of any information it contains.

This work demonstrates a rare earth (RE) valve manipulation to address the persistent activity-selectivity trade-off in heterogeneous catalysis, where RE function as dynamic reaction modulators rather than passive components. Unlike existing RE-modified catalysts that are limited to electron transfer, our PtCoCe alloy employ Ce's 4f-5d orbital hybridization as an electronic switch to optimize Pt d-band centers, while the ionic radius serves as a geometric regulator that sterically distorts intermediates. Crucially, although the oxophilicity of RE typically hinders alloy synthesis, we leverage the negative formation energy of RE alloys to enhance surface stabilization. By capitalizing on this synergistic regulation, the catalyst achieves exceptional semi-hydrogenation performance of phenylacetylene under mild conditions, effectively overcoming the inherent reactivity-selectivity trade-off associated with precious metal systems. These breakthroughs establish that: (1) 4f orbitals can covalently hybridize with transition metals to govern bond activation pathways; (2) Ionic radii provide atomic-scale steric control that extends beyond traditional strain effects; and (3) The integration of RE elements introduces two new tunable parameters (orbital coupling and spatial constraint) for precision catalyst design, thereby opening new avenues for manipulating multistep reactions beyond hydrogenation.

View Article Online  
DOI: 10.1039/D5MH01041A

*Data availability statements*

View Article Online  
DOI: 10.1039/D5MH01041A

# Rare Earth Valve Manipulated Dual Regulation of Electronic States and Adsorption Geometry in the Selective Hydrogenation of Phenylacetylene

Kunhong Jiang, Yong Jiang, Zhong Liang, Wenshuo Zhang, Hengjun Liu, Jiali Shi,  
Siyuan Wang, Ziyun Zhong, and Yaping Du\*

The data supporting this article have been included as part of the Supplementary Information.

# Rare Earth Valve Manipulates Dual Regulation of Electronic States and Adsorption Geometry in the Selective Hydrogenation of Ethynylbenzene

Received 00th January 20xx,  
Accepted 00th January 20xx

DOI: 10.1039/x0xx00000x

Kunhong Jiang,<sup>a</sup> Yong Jiang,<sup>a</sup> Zhong Liang,<sup>a</sup> Wenshuo Zhang,<sup>a</sup> Hengjun Liu,<sup>a</sup> Jiali Shi,<sup>a</sup> Siyuan Wang,<sup>a</sup> Ziyun Zhong,<sup>a</sup> and Yaping Du<sup>\*a</sup>

The semi-hydrogenation of ethynylbenzene is a fundamental reaction in the synthesis of polymer precursors. However, achieving a balance between catalytic activity and styrene selectivity remains a significant challenge due to the risk of over-hydrogenation. Herein, we design ternary Pt<sub>2-x</sub>Co<sub>x</sub>Ce rare earth alloys to synergistically regulate electronic states and adsorption geometries, thereby enhancing selective hydrogenation. The optimized Pt<sub>1.5</sub>Co<sub>0.5</sub>Ce catalyst exhibits remarkable performance, achieving a 98.3% conversion of ethynylbenzene, an 85.1% selectivity for styrene, and a turnover frequency (TOF) of 1549.6 h<sup>-1</sup> under mild conditions, surpassing most reported Pt-based catalysts. In situ spectroscopy, combined with kinetic analysis, demonstrates that the catalyst facilitates the adsorption and conversion of ethynylbenzene. Density functional theory (DFT) calculations reveal that directional electron transfer from Ce (4f) to Pt/Co (5d) via d-f orbital hybridization effectively modulates the position of the Pt d-band center, weakening the over-adsorption of the intermediate styrene while preserving optimal activation of ethynylbenzene. Additionally, the large ionic radius of Ce spatially alters the adsorption configuration of styrene, reducing its adsorption energy and increasing the energy barrier to suppress ethylbenzene formation. This study illustrates that rare earth alloy engineering is a universal strategy to address the activity-selectivity trade-off in heterogeneous catalysis.

## Introduction

As a cornerstone of industrial chemistry, styrene supports the synthesis of polymers, pharmaceuticals, and engineered pigments.<sup>1-5</sup> However, styrene derived from naphtha cracking typically contains about 1% ethynylbenzene, which poisons the polymerization catalysts and reduce the quality of polymers.<sup>6-8</sup> Consequently, the selective hydrogenation of ethynylbenzene to styrene is of great importance and has attracted particular attention in both the academia and chemical industry, especially relevant to commodity chemical production.<sup>9-11</sup> Nevertheless, ethynylbenzene could bind strongly to catalysts surfaces due to triple bond, causing high surface coverage that blocks active sites, limiting H<sub>2</sub> activation and slowing reaction kinetics.<sup>12,13</sup> Furthermore, the strong alkene-binding on the catalyst surface affinity extends intermediate surface residence time, inevitably leading to over-hydrogenation, suffer from the inherent activity-selectivity trade-offs.<sup>14-16</sup> Therefore, the rational design of selective ethynylbenzene hydrogenation catalysts with high activity, selectivity and stability has become the focus of attention.

It is difficult to achieve high selectivity for styrene due to the fact that the olefin product (styrene) is more prone to undergo further hydrogenation reactions than the alkene substrate (ethynylbenzene).<sup>17, 18</sup> To optimize catalytic performance for the highly challenging semi-hydrogenation of ethynylbenzene to styrene, the surface architecture of catalysts requires meticulous design to

either lower binding energy/surface coverage or spatially isolate adsorbed molecules, thereby suppressing undesirable side reactions. Various selective regulation strategies have been developed to address this limitation. For instance, poisoning or ligand modification by adding toxic substances (Pb in Lindlar catalysts) or organic ligands can generate a "site-blocking" effect, reduce contiguous active sites and suppress over-hydrogenation.<sup>19, 20</sup> Additionally, support engineering involves using supports with oxygen vacancies (CeO<sub>2</sub> support) or nitrogen-doped carbon materials to modulate metal-support interaction and enhance preferential adsorption of ethynylbenzene over styrene.<sup>21, 22</sup> Nevertheless, maintaining the environmental compatibility and long-term stability of catalysts through controlled carrier sintering or ligand leaching during reaction processes remains a significant challenge. Recent advances in catalyst design have focused on more fundamental tailoring electronic and geometric structures to enhance activity and selectivity in hydrogenation catalysis.<sup>23-29</sup> Electronic modulation through noble-transition metal alloys can modulate electronic properties, creating isolated active sites with tailored adsorption strengths. For instance, alloying Pt with transition metals Cd generates reconstructed Pt-Cd surfaces that shift the d-band center downward compared to pure Pt, weakening adsorption interactions and enhancing styrene selectivity.<sup>30</sup> Geometric engineering strategies, such as anchoring cobaltocene cobalt organometallic fragments (CpCo) on Pt/SiO<sub>2</sub> interfaces, induce interfacial charge transfer to form electron-rich Pt sites, which suppress over-hydrogenation.<sup>31</sup> The strategic regulation of transition metal alloying in Pt-based catalysts is a critical way for optimizing both electronic and geometric configurations, so that the adsorption strength and spatial

<sup>a</sup> Tianjin Key Lab for Rare Earth Materials and Applications, Center for Rare Earth and Inorganic Functional Materials, Smart Sensing Interdisciplinary Science Center, School of Materials Science and Engineering, National Institute for Advanced Materials, Nankai University  
Tianjin 300350, P. R. China  
E-mail: ypdu@nankai.edu.cn

Electronic supplementary information available: [details of any supplementary information available should be included here]. See DOI: 10.1039/x0xx00000x

distribution of reaction intermediates can be precisely controlled. Consequently, developing tailored alloy architectures to enhance hydrogenation selectivity and activity represents a pivotal topic in selective hydrogenation catalysis.

Rare earth (RE) elements have emerged as pivotal components in advanced catalysis due to their special 4f electron configuration, which can modulate the interaction between active sites and intermediates as electron buffer in specific catalytic systems.<sup>32-34</sup> The unique physicochemical properties of RE elements, including large ionic radius, flexible coordination environments, and variable valence states, endowing them with unparalleled capabilities as catalytic promoters.<sup>35-37</sup> Recent research advances demonstrate that regulation of RE 4f electrons can substantially enhance activity and selectivity. Specifically, constructing d-f electron transition ladders to facilitate charge transfer, while establishing gradient 3d-2p-4f such as Ce(4f)-O(2p)-Co(3d) electronic units to optimize \*O and \*OH intermediate adsorption and in turn enhance the OER activity.<sup>38, 39</sup> In addition, engineering d-f orbital hybridization to modify electronic structures and surface-bound intermediates, leading to an optimized catalytic selectivity, and promoting 4f electron delocalization synergistically optimize adsorption energetics of reactive intermediates to reduce activation barriers.<sup>40-42</sup> Crucially, RE alloys enable precise tuning of d-f orbital coupling strength while maintaining robustness under harsh catalytic conditions.<sup>43, 44</sup> Building on these advancements, we propose that the rational integration of 4f electron characteristics through the tailored RE alloys catalyst design could release novel electronic synergies in selective hydrogenation reactions, thereby developing high-performance and low-cost alternatives to traditional noble metal systems.

Guiding by these principles, we firstly develop ternary Pt-Co-Ce RE alloys that integrate 4f orbital hybridization with geometric modulation. The prepared catalyst achieves an exceptional balance between catalytic activity and styrene selectivity. Under mild conditions, the ethynylbenzene conversion rate is 98.3%, the styrene selectivity is 85.1%, and the turnover frequency (TOF) was 1549.6 h<sup>-1</sup>, surpassing most reported Pt-based catalysts. Through synergistic electronic-geometric design, in situ characterization and theoretical analyses reveal a dual-regulation mechanism. Directional electron transfer via d-f hybridization modulates the Pt d-band center to differentially activate reactants while suppressing intermediate over-adsorption. Meanwhile, the large ionic radius of RE elements induces steric distortion that alters the geometry of intermediates, reducing adsorption energy and elevating the energy barrier for ethylbenzene formation, thereby breaking the activity-selectivity trade-off. The demonstrated electronic-geometric cooperativity opens avenues for the utilization of 4f orbital characteristics in heterogeneous catalysis, particularly for reactions requiring simultaneous control of adsorption energetics and spatial configurations.

## Results and Discussion

The ternary Pt<sub>2-x</sub>Co<sub>x</sub>Ce alloy was prepared using the sodium vapor reduction method as shown in Figure 1a and Supporting Information. Among them, chloroplatinic acid hexahydrate, cerous chloride, cobalt chloride hexahydrate, cyanamide, and carbon black were used

as metal precursors, dispersant, and carriers, respectively. During thermal activation, CN<sub>2</sub>H<sub>2</sub> acts as a bifunctional agent that not only facilitates the formation of a g-C<sub>3</sub>N<sub>4</sub> network to confine nanoparticle growth but also creates a reducing atmosphere to accelerate reduction kinetics.<sup>45, 46</sup> The Pt<sub>2-x</sub>Co<sub>x</sub>Ce nanoalloy was obtained by annealing the mixture with Na vapor at 600 °C for 2 h in an argon atmosphere. The resulting mixture was washed with isopropanol to remove residual sodium metal and then acid-etched to obtain the carbon-supported Pt<sub>2-x</sub>Co<sub>x</sub>Ce catalyst (referred to as Pt<sub>2-x</sub>Co<sub>x</sub>Ce/C, x = 0, 0.2, 0.5, 0.8, 1.0). Furthermore, by adjustment of the Co/Pt ratio in the raw materials, the stoichiometric ratio of Co in Pt<sub>2-x</sub>Co<sub>x</sub>Ce nanoparticles (NPs) could be controlled. The Pt/C, PtCo/C (Pt/Co molar ratio of 1:1), catalyst was also prepared for comparison using the same conditions, except that no RE elements were added. The Pt/Co/Ce molar compositions of synthesized samples were determined by inductively coupled plasma optical emission spectroscopy (ICP-OES) (Table S1).

The crystalline phase structure of the synthesized catalysts was characterized by X-ray diffraction (XRD) (Figure 1b). For Ce-free samples, Pt/C shows diffraction peaks matching the face-centered cubic (fcc) Pt reference (PDF#04-0802), while PtCo/C is consistent with PtCo (PDF#65-8970). The Ce-containing Pt<sub>2</sub>Ce/C displays distinct peaks at 19.9°, 32.9°, 38.7°, 40.5°, and 47.1°, indexed to the (111), (220), (311), (222), and (400) planes of cubic Pt<sub>2</sub>Ce (PDF#17-0010), indicating the formation of Pt-Ce alloys.<sup>47</sup> The XRD patterns of different Pt<sub>2-x</sub>Co<sub>x</sub>Ce/C catalysts display that all of the diffraction peaks are close to those observed in Pt<sub>2</sub>Ce, revealing the successful formation of trimetallic PtCoCe/C alloy structure. In addition, the diffraction peaks of Pt<sub>2-x</sub>Co<sub>x</sub>Ce/C shifts slightly to higher diffraction angles compared to those of Pt<sub>2</sub>Ce/C (Figure S1), which indicates lattice contraction due to the introduction of Co atoms in the crystal framework.<sup>48</sup> The structures evolution is further confirmed by Rietveld refinement of the XRD patterns (Figures 1c and S2). The quantitative lattice parameters (Table S2) reveal a reduction in unit cell volume from 445.9 Å<sup>3</sup> (Pt<sub>2</sub>Ce) to 439.0 Å<sup>3</sup> (Pt<sub>1.5</sub>Co<sub>0.5</sub>Ce/C), directly evidencing the lattice distortion induced by Co incorporation. The refinement results explicitly demonstrate that Co partially replaces Pt at the tetrahedral sites of the alloy framework, while Ce atoms remain anchored at the eight corner positions of the unit cell (Figure 1d). The morphology and dispersion of the obtained Pt, PtCo and Pt<sub>2-x</sub>Co<sub>x</sub>Ce alloys NPs were systematically analyzed by transmission electron microscopy (TEM) analysis. As shown in Figure S3, the metal nanoparticles over all catalysts are highly dispersed on the carbon support without aggregation. The metal particle size of the Pt<sub>1.5</sub>Co<sub>0.5</sub>Ce/C is 6.62 nm, which is similar to those of Pt/C, PtCo/C, Pt<sub>1.0</sub>Co<sub>1.0</sub>Ce/C, Pt<sub>1.2</sub>Co<sub>0.8</sub>Ce/C, Pt<sub>1.8</sub>Co<sub>0.2</sub>Ce/C and Pt<sub>2</sub>Ce/C catalysts, (particle sizes mainly range from 6.62 to 6.72 nm). Furthermore, the Brunauer-Emmett-Teller (BET) surface areas of Pt/C, Pt<sub>2</sub>Ce/C, Pt<sub>1.5</sub>Co<sub>0.5</sub>Ce/C, Pt<sub>1.0</sub>Co<sub>1.0</sub>Ce/C, and PtCo/C are 373.20 m<sup>2</sup>/g, 350.53 m<sup>2</sup>/g, 346.39 m<sup>2</sup>/g, 329.72 m<sup>2</sup>/g, and 349.41 m<sup>2</sup>/g, respectively (Figure S4 and Table S3). These similar BET surface areas results confirm the uniformity of metal particle dispersion, indicating that the size of metal

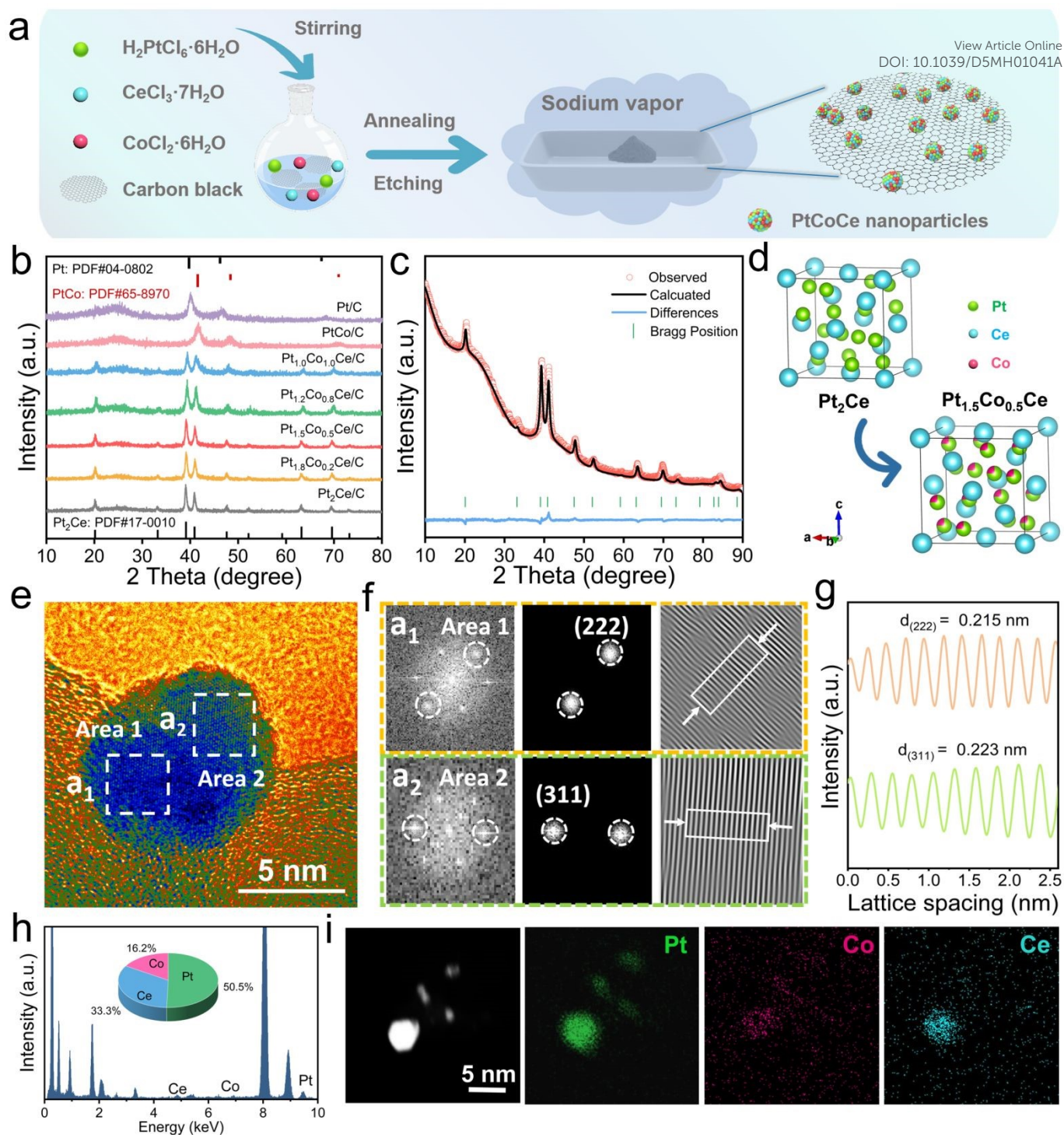


**Figure 1** (a) Schematic illustration of the synthesis process for Pt<sub>2-x</sub>Co<sub>x</sub>Ce/C. (b) XRD patterns of Pt<sub>2-x</sub>Co<sub>x</sub>Ce/C series samples. (c) Rietveld refinement for the XRD pattern of Pt<sub>1.5</sub>Co<sub>0.5</sub>Ce/C. (d) Atomic crystal structures of Pt<sub>2</sub>Ce and Pt<sub>1.5</sub>Co<sub>0.5</sub>Ce/C. (e) HRTEM image of Pt<sub>1.5</sub>Co<sub>0.5</sub>Ce/C. (f) The corresponding FFT and inverse FFT patterns of (a<sub>1</sub>: Area 1) and (a<sub>2</sub>: Area 2) in (e). (g) Intensity profiles from the white area in (f). (h) STEM-EDX spectra and (i) elemental mappings images of Pt<sub>1.5</sub>Co<sub>0.5</sub>Ce/C, showing the distributions of Pt (green), Co (pink), and Ce (blue).

particles in each sample are statistically comparable. This morphological consistency across the alloy series eliminates particle shape/size effects as confounding variables, enabling focused investigation of the resolution TEM (HRTEM) and scanning TEM energy-dispersive X-ray spectra (STEM-EDX) results corroborate the successful synthesis of Pt<sub>2</sub>Ce and PtCo alloy phases, as evidenced by lattice fringe matching to

reference and uniform elemental distribution (Figures S5 and S6). For the Pt<sub>1.5</sub>Co<sub>0.5</sub>Ce catalyst, HRTEM image reveals high crystallinity with ordered lattice arrangements (Figure 1e), verified by the corresponding fast Fourier transform (FFT) patterns (Figure 1f). Furthermore, the inverse FFT (IFFT) patterns and the corresponding integrated pixel intensities display the lattice spacing with 0.215 and 0.223 nm

corresponds to the (222) and (311) planes of  $\text{Pt}_2\text{Ce}$ , respectively (Figure 1g). Meanwhile, these spacings are slightly composition-dependent structure-activity relationships in RE alloy systems. The high-smaller than that of  $\text{Pt}_2\text{Ce}$ , which is owing to the lattice shrinkage caused by the difference in ionic radii between Pt (0.62 Å) and Co (0.54 Å),<sup>49</sup> in agreement with XRD patterns. The atomic ratio of Pt/Co/Ce in  $\text{Pt}_{1.5}\text{Co}_{0.5}\text{Ce}/\text{C}$  is determined to be

1/0.32/0.65 by STEM-EDX (Figure 1h), showing stoichiometric consistency with ICP-OES measurements. Moreover, the elemental mappings of  $\text{Pt}_{1.5}\text{Co}_{0.5}\text{Ce}/\text{C}$  catalyst provide the additional confirmation of uniform distribution of Pt, Co and Ce elements throughout the entire NPs, thereby supporting the formation of trimetallic PtCoCe catalysts (Figure 1i).

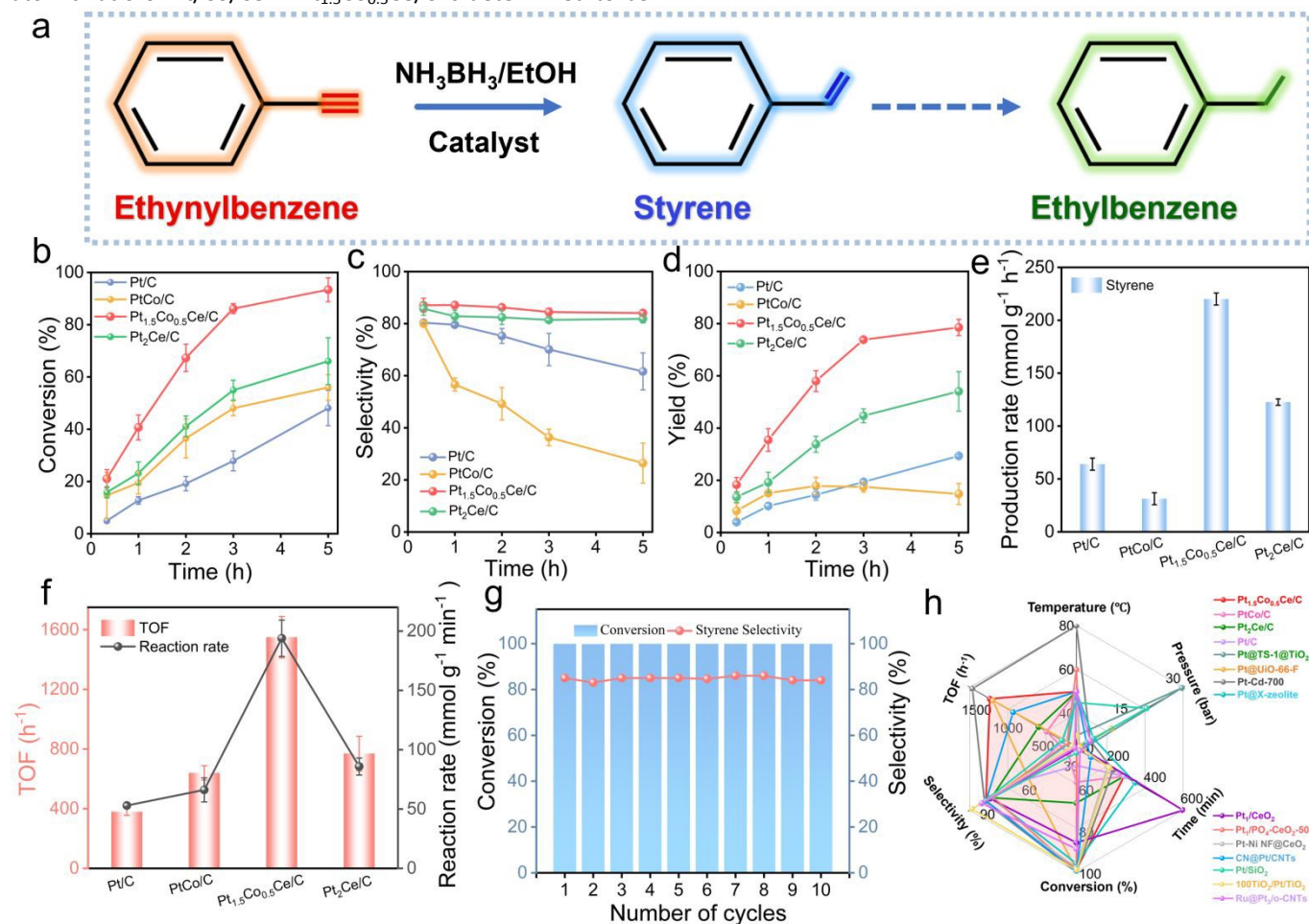


**Figure 2** Catalytic performance for ethynylbenzene hydrogenation over Pt/C, PtCo/C,  $\text{Pt}_{1.5}\text{Co}_{0.5}\text{Ce}/\text{C}$ , and  $\text{Pt}_2\text{Ce}/\text{C}$  catalysts. (a) Schematic of ethynylbenzene hydrogenation reaction. (b) Time-dependent conversion of the hydrogenation of ethynylbenzene. Reaction conditions: 1.0 mmol ethynylbenzene, 4 mL ethanol, 323 K, 3 mg catalyst, 2.50 mmol/mL  $\text{NH}_3\text{BH}_3$ . (c) Styrene selectivity and (d) Styrene yield with time on stream. (e) Production rate of styrene at 5 h. (f) TOF and reaction rate values of ethynylbenzene hydrogenation at an initial 20 min. (g) The stability test of  $\text{Pt}_{1.5}\text{Co}_{0.5}\text{Ce}/\text{C}$  for 5 h. (h) Comparison of  $\text{Pt}_{1.5}\text{Co}_{0.5}\text{Ce}/\text{C}$  and other reported Pt-based catalysts for the selective hydrogenation of ethynylbenzene (Table S5).

To elucidate the structure-activity relationship of the  $\text{Pt}_x\text{Co}_x\text{Ce}/\text{C}$  alloy system ( $x = 0.2, 0.5, 0.8, 1.0$ ), we systematically evaluated the catalytic performance of the catalysts for ethynylbenzene semi-hydrogenation by using  $\text{NH}_3\text{BH}_3$  as a hydrogen donor under mild conditions (1.00 mmol ethynylbenzene, 4.00 mL ethanol, 323.00 K, 3.00 mg catalyst, 2.50 mmol/mL  $\text{NH}_3\text{BH}_3$ ) (Figure 2a). A volcano-shaped activity trend emerged with Co content variation (Figure S7), where  $\text{Pt}_{1.5}\text{Co}_{0.5}\text{Ce}/\text{C}$  ( $x = 0.5$ ) achieved conversion above 98% within 5 h. The time-dependent conversion profiles (Figure 2b) further demonstrate the superior activity of  $\text{Pt}_{1.5}\text{Co}_{0.5}\text{Ce}/\text{C}$ , significantly outperforming  $\text{Pt}_2\text{Ce}/\text{C}$  (66.0%), PtCo/C (55.9%), and Pt/C (48.1%) under the same conditions. The enhanced catalytic activity of  $\text{Pt}_{1.5}\text{Co}_{0.5}\text{Ce}/\text{C}$  highlights an optimized balance of

geometric and electronic effects conferred by controlled Co incorporation, combined with the synergistic interplay of Pt, Co, and Ce within the alloy structure. In addition, the effect of  $\text{NH}_3\text{BH}_3$  amount (0.41-0.33 mmol/mL) on the ethynylbenzene hydrogenation performance is also discussed (Figure S8), and the optimal addition amount is 2.50 mmol/mL. Meanwhile, solvent screening identifies ethanol as optimal for maximizing both conversion and styrene selectivity over  $\text{Pt}_{1.5}\text{Co}_{0.5}\text{Ce}/\text{C}$  (Table S4). Notably,  $\text{Pt}_{1.5}\text{Co}_{0.5}\text{Ce}/\text{C}$  maintains above 85% selectivity of styrene with high ethynylbenzene conversion at 5 h (Figure 2c), outperforming Pt/C (61.6%), PtCo/C (26.4%), and  $\text{Pt}_2\text{Ce}/\text{C}$  (81.8%) while suppressing ethylbenzene formation. This contrasts sharply with the rapid selectivity degradation observed in PtCo/C

and structural modulation. The catalytic performance of Pt<sub>1.5</sub>Co<sub>0.5</sub>Ce/C is characterized by a product distribution dominated by styrene, achieving an 80.0% yield with a remarkable productivity rate of 230.1 mmol g<sup>-1</sup> h<sup>-1</sup>, with minimal ethylbenzene formation (Figure 2d, e). The catalytic efficiency was further quantified through intrinsic reaction rate calculations and turnover frequency (TOF) (Figure 2f), Pt<sub>1.5</sub>Co<sub>0.5</sub>Ce/C delivers a hydrogenation reaction rate of 193.9 mmol g<sup>-1</sup> min<sup>-1</sup>. Simultaneously, the catalyst exhibits an ultrahigh TOF value of 1549.6 h<sup>-1</sup>, which was 4.1, 2.4, and 2.0 times higher than that of Pt/C (379.3 h<sup>-1</sup>), PtCo/C (640.0 h<sup>-1</sup>), and Pt<sub>2</sub>Ce/C (769.8 h<sup>-1</sup>), respectively. Recyclability tests under optimal conditions demonstrate outstanding stability, with Pt<sub>1.5</sub>Co<sub>0.5</sub>Ce/C retains > 95% conversion and > 85% styrene selectivity over 10 cycles (Figure 2g). The XRD pattern of the used Pt<sub>1.5</sub>Co<sub>0.5</sub>Ce/C exhibits high crystallinity, suggesting no significant structural changes (Figure S9). The TEM shows that the NPs are uniformly dispersed within the used Pt<sub>1.5</sub>Co<sub>0.5</sub>Ce/C (Figure S10), with a particle size distribution of approximately 6.87 nm. Furthermore, distinct lattice fringes corresponding to the (311) crystal plane is clearly observed in HRTEM images. Elemental mapping analysis indicates that the constituent elements are uniformly distributed, suggesting no detectable phase separation. These observations collectively demonstrate the prominent stability of RE alloy catalysts. Significantly, the catalytic performance of Pt<sub>1.5</sub>Co<sub>0.5</sub>Ce/C is higher than that of most platinum group metal-based catalysts reported thus far (Figure 2h, Table S5). The outstanding performance stems from the synergistic interplay of optimized composition and structure. Specifically, Co and Ce incorporation modulates the electronic properties of Pt active sites, enhancing selective hydrogenation of the C≡C bond in ethynylbenzene to the C=C bond in styrene. Additionally, the presence of Ce promotes the stability and dispersion of the active metal sites, further contributing to the catalyst's high selectivity and productivity.

To further elucidate the superior catalytic performance of Pt<sub>1.5</sub>Co<sub>0.5</sub>Ce/C catalyst in ethynylbenzene hydrogenation, systematic kinetic analyses were performed. Initial reaction rate data collected at different temperatures facilitated the construct of Arrhenius plots (Figures 3a and S11), which illustrated the ln(rate) versus 1/T relationship.<sup>50</sup> Arrhenius analysis reveals a substantial reduction in apparent activation energy ( $E_a$ ) from 30.79 kJ·mol<sup>-1</sup> (Pt/C) to 14.82 kJ·mol<sup>-1</sup> (Pt<sub>1.5</sub>Co<sub>0.5</sub>Ce/C), demonstrating effective energy barrier lowering through rare-earth alloy engineering. Notably, the binary PtCo/C exhibits intermediate  $E_a$  (26.01 kJ·mol<sup>-1</sup>), highlighting the critical role of Ce in modulating the energy landscape of the rate-limiting step.<sup>51, 52</sup> To investigate the factors governing the reaction pathway in hydrogenation reaction, subsequent evaluation of reaction orders was conducted through ethynylbenzene concentration variation (Figure S12), which demonstrates distinct adsorption characteristics.<sup>51, 53</sup> The calculated reaction orders of 0.26 (Pt/C), 0.22 (PtCo/C), and 0.17 (Pt<sub>1.5</sub>Co<sub>0.5</sub>Ce/C) suggest progressively stronger substrate adsorption on the Pt<sub>1.5</sub>Co<sub>0.5</sub>Ce/C RE alloy catalyst surface (Figure 3b), thereby enhancing activation efficiency and pathway selectivity. To clarify the mechanistic

origin of the enhanced selectivity in Pt<sub>1.5</sub>Co<sub>0.5</sub>Ce/C, we performed comparative hydrogenation tests using styrene as a probe reaction. As shown in Figure 3c, the conversion rate reveals a 3.1-fold lower conversion over Pt<sub>1.5</sub>Co<sub>0.5</sub>Ce/C catalyst (24.7%) compared to PtCo/C (76.2%), demonstrating significant suppression of styrene hydrogenation on the ternary RE alloy catalyst. This significant difference highlights the key role of Ce integration in reducing the adsorption strength of styrene intermediates and effectively inhibiting their excessive hydrogenation to ethylbenzene. In situ diffuse reflectance infrared Fourier transform spectroscopy (In situ DRIFTS) was employed to dynamically monitor the ethynylbenzene hydrogenation processes over Pt<sub>1.5</sub>Co<sub>0.5</sub>Ce/C, PtCo/C, and Pt/C catalysts. For Pt<sub>1.5</sub>Co<sub>0.5</sub>Ce/C, the characteristic C≡C stretching vibration of ethynylbenzene at 2150 cm<sup>-1</sup> gradually disappears with increasing reaction time,<sup>54</sup> accompanied by the emergence of a C=C stretching band (1630 cm<sup>-1</sup>) within 5 minutes,<sup>55, 56</sup> confirming rapid and selective hydrogenation to styrene (Figure 3d, d<sub>1</sub>-d<sub>2</sub>). In contrast, PtCo/C exhibits sluggish C≡C bond activation coupled with rapid attenuation of the styrene signal (C=C), indicative of inefficient ethynylbenzene conversion followed by over-hydrogenation to ethylbenzene (Figure 3e, e<sub>1</sub>-e<sub>2</sub>). Notably, the Pt/C catalyst displays negligible activity, with neither C≡C consumption nor C=C formation observed, reflecting its limited capacity for both hydrogen dissociation and product accumulation (Figure 3f, f<sub>1</sub>-f<sub>2</sub>). These spectroscopic results conclusively demonstrate that the ethynylbenzene hydrogenation process proceeds most efficiently on the Pt<sub>1.5</sub>Co<sub>0.5</sub>Ce/C catalyst, with PtCo/C and Pt/C exhibiting progressively inferior catalytic performance. To further clarify the diversity of the hydrogenation performance of Pt<sub>1.5</sub>Co<sub>0.5</sub>Ce/C, we expanded the range of reaction substrates under the same ethynylbenzene semi-hydrogenation conditions (Figures S13, S14, Table S6), demonstrating the wide applicability in hydrogenation reactions of other functional groups.

X-ray photoelectron spectroscopy (XPS) was conducted to elucidate the electronic interactions and charge transfer mechanisms within PtCo/C, Pt<sub>2</sub>Ce/C and Pt<sub>2-x</sub>Co<sub>x</sub>Ce/C RE alloy systems. The Pt 4f XPS spectrum of these catalysts can be deconvoluted into two sets of doublets peaks, corresponding to the 4f<sub>7/2</sub> and 4f<sub>5/2</sub> electronic orbitals of Pt<sup>0</sup> and Pt<sup>2+</sup> (Figure 4a). Notably, compared to the Pt 4f binding energy of Pt/C (71.8 eV for 4f<sub>7/2</sub>), the binding energies of PtCo/C, Pt<sub>2</sub>Ce/C, Pt<sub>1.8</sub>Co<sub>0.2</sub>Ce/C, and Pt<sub>1.5</sub>Co<sub>0.5</sub>Ce/C exhibited negative shifts of 0.2, 0.2, 0.3, and 0.4 eV, respectively, demonstrating that a large number of electrons are transferred to Pt sites in the alloy.<sup>57</sup> This systematic decrease in binding energy indicates a progressive electron enrichment at Pt sites, attributed to electron donation from less electronegative Co (electronegativity = 1.88) and Ce (1.12) to Pt (2.28) within the alloy systems,<sup>58, 59</sup> where Pt<sub>1.5</sub>Co<sub>0.5</sub>Ce/C exhibits the highest electron density at Pt sites. Typically, Pt<sup>2+</sup> gradually converted to Pt<sup>0</sup> species as Co and Ce incorporation, giving rise to the highest Pt<sup>0</sup> fraction of ≈71.6% in Pt<sub>1.5</sub>Co<sub>0.5</sub>Ce/C (Figure 4b). The Co 2p XPS spectrum of PtCo/C, Pt<sub>1.5</sub>Co<sub>0.5</sub>Ce/C and Pt<sub>1.8</sub>Co<sub>0.2</sub>Ce/C can be divided into three distinct groups of peaks attributed to the 2p<sub>3/2</sub> and 2p<sub>1/2</sub> orbits of Co<sup>0</sup>, Co<sup>2+</sup> and the satellite peaks (Figure 4c). The PtCo/C display

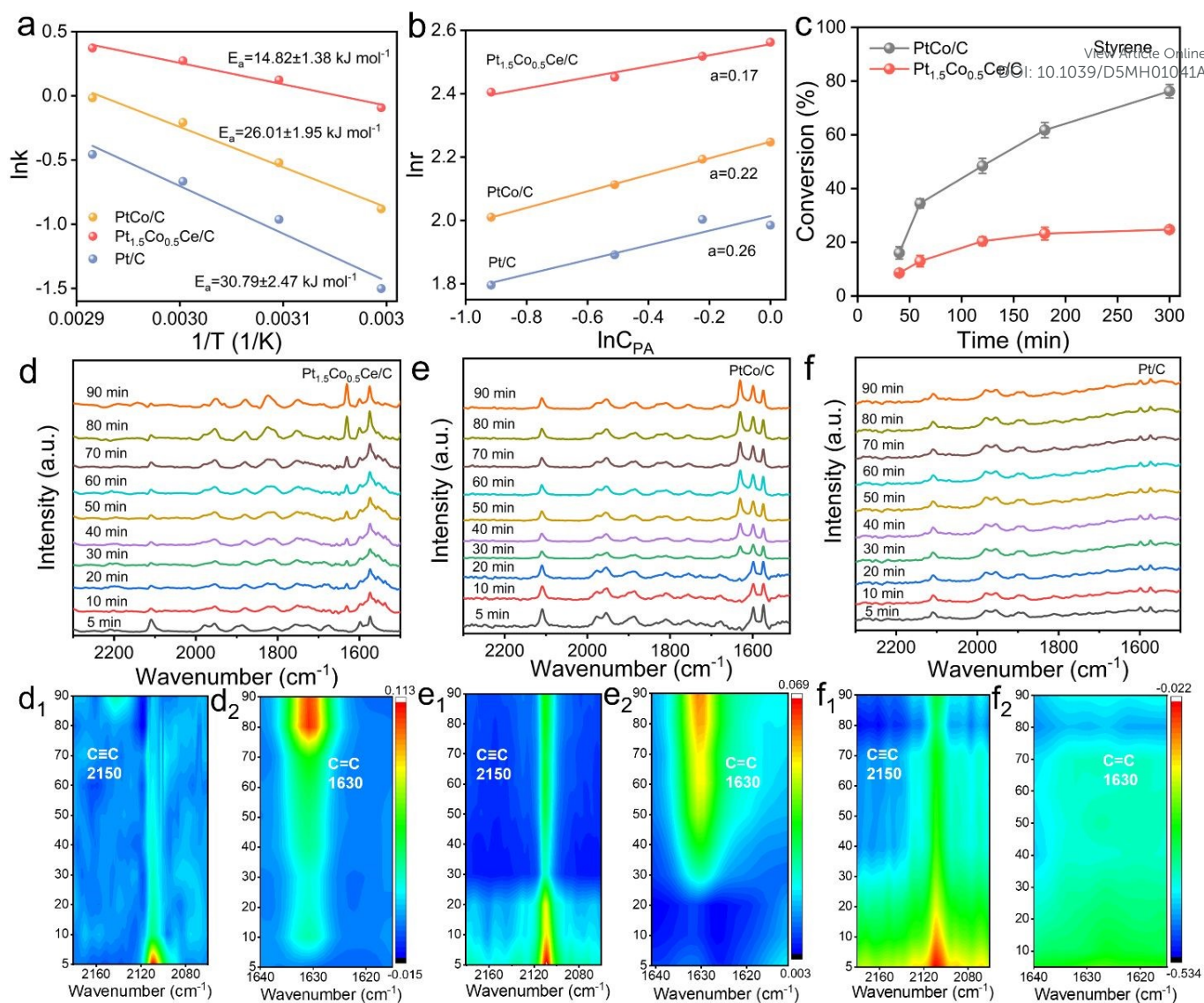


**Figure 3** (a) Apparent activation energies ( $E_a$ ) for the hydrogenation of ethynylbenzene and styrene over Pt/C, PtCo/C, Pt<sub>1.5</sub>Co<sub>0.5</sub>Ce/C, and Pt<sub>2</sub>Ce/C. (b) Fitting lines with the reaction order of ethynylbenzene over Pt/C, PtCo/C, Pt<sub>1.5</sub>Co<sub>0.5</sub>Ce/C. (c) Product distribution of styrene hydrogenation reaction under the conditions of styrene solution over PtCo/C and Pt<sub>1.5</sub>Co<sub>0.5</sub>Ce/C. Spectra and contour maps of (d, d<sub>1</sub>-d<sub>2</sub>) Pt<sub>1.5</sub>Co<sub>0.5</sub>Ce/C, (e, e<sub>1</sub>-e<sub>2</sub>) PtCo/C, (f, f<sub>1</sub>-f<sub>2</sub>) Pt/C recorded during hydrogenation of ethynylbenzene at 353.0 K.

(reduced by 53.6%) and Pt/C (reduced by 18.7%) under identical conditions, directly evidencing Ce's critical role in inhibiting over-hydrogenation through electronic three components with the binding energies of Co<sup>0</sup> (779.1 eV for 2p<sub>3/2</sub> and 794.6 eV for 2p<sub>1/2</sub>), Co<sup>2+</sup> (782.1 eV for 2p<sub>3/2</sub> and 797.9 eV for 2p<sub>1/2</sub>), and satellite peaks. It is worth noting that the Co<sup>0</sup> 2p<sub>3/2</sub> binding energy in Pt<sub>1.5</sub>Co<sub>0.5</sub>Ce/C shows a negative shift of 0.5 eV (778.6 eV) compared to PtCo/C, and the Co<sup>0</sup> fraction is approximately 58.9% (Figure 4d), suggesting electron accumulation at Co sites. This contrasts with PtCo/C, where weaker Co-Pt interactions restrict the redistribution of electrons, while the ternary alloy system facilitates enhanced charge transfer through synergistic Co-Ce-Pt interactions, thereby improving catalytic.<sup>60, 61</sup> The Ce 3d spectra (Figure 4e) exhibit spin-orbit split peaks at 904.8 eV (Ce 3d<sub>3/2</sub>) and 886.5 eV (Ce 3d<sub>5/2</sub>), characteristic of metallic Ce<sup>0</sup> these alloys. Additionally, the binding energy of the Ce 3d<sub>5/2</sub> in Pt<sub>1.5</sub>Co<sub>0.5</sub>Ce/C (886.7 eV) and Pt<sub>1.0</sub>Co<sub>1.0</sub>Ce/C (887.0 eV) exhibits positive shift of +0.2 and +0.5 eV compared to Pt<sub>2</sub>Ce/C (886.5 eV). This is due to the electron transfer from Ce atoms to the

neighboring Pt/Co atoms, resulting in a decrease of electron density around Ce. Two additional low-intensity peaks at 901.5 eV (Ce 3d<sub>3/2</sub>) and 883.2 eV (Ce 3d<sub>5/2</sub>) may be caused by the transfer of electrons from Ce to Pt and Co. The XPS valence band spectra of PtCe and PtCoCe catalysts show that the trend of electron density intensity near the Fermi level ( $E_F$ ) for the samples is Pt<sub>2</sub>Ce/C > Pt<sub>1.5</sub>Co<sub>0.5</sub>Ce/C > Pt<sub>1.0</sub>Co<sub>1.0</sub>Ce/C, with Pt<sub>2</sub>Ce/C exhibiting the highest value (Figure S15). Meanwhile, the d-band of PtCoCe catalysts are altered by valence electrons near  $E_F$  (Figure S16). These results highlight the critical role of Ce in increasing electron density at Pt/Co sites and enhancing electron conduction. These observations corporately reveal that there is a significant electronic effect in the PtCoCe alloy, where Ce acting as a primary electron donor to both Pt and Co. The (splitting energy = 18.3 eV).<sup>62</sup> This splitting value aligns with metallic cerium, confirming the dominant metallic valence state of Ce in XPS comparative analysis of the states of the catalyst before and after the reaction shows that the electronic structure of the elements

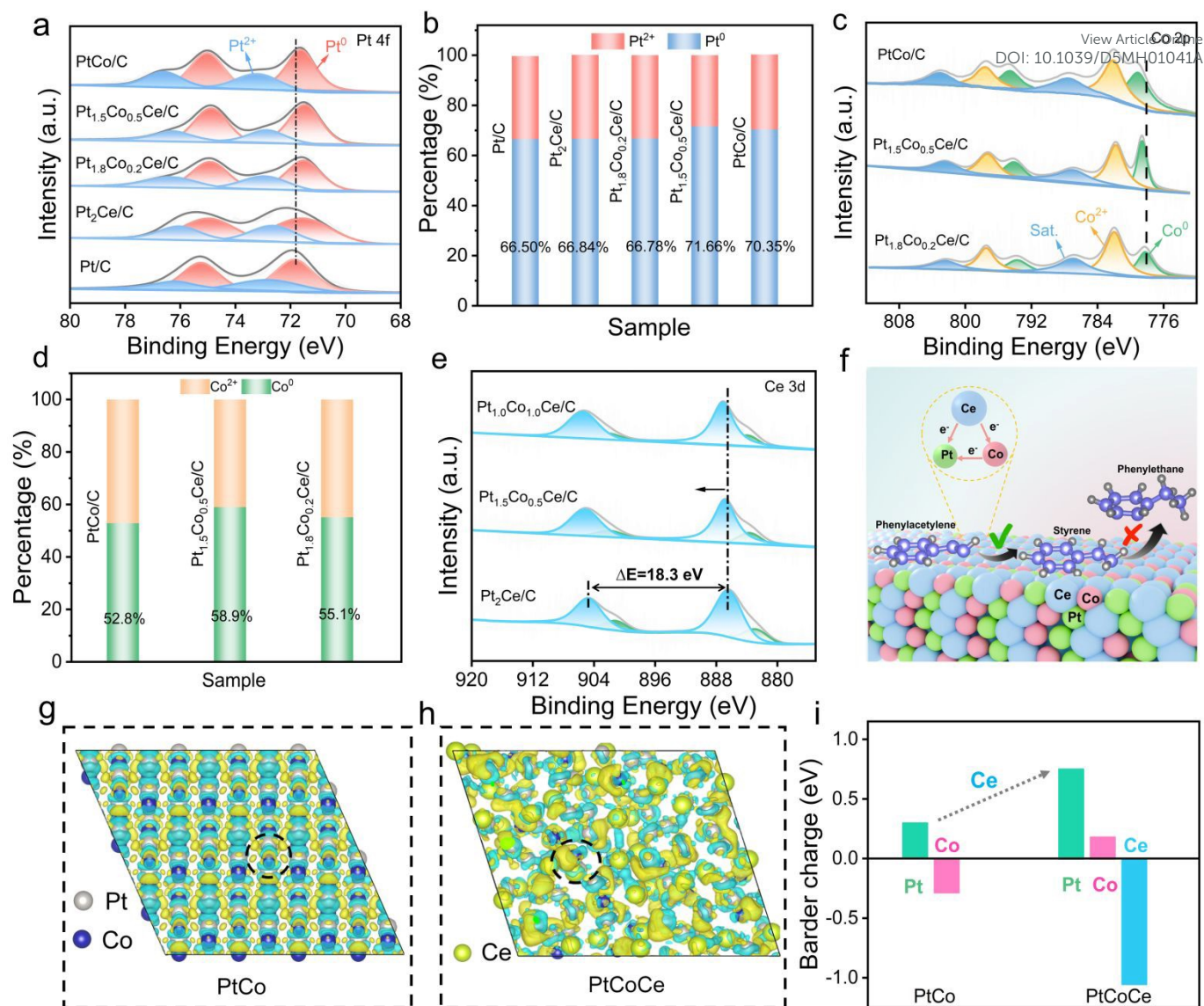


**Figure 4** (a) Pt 4f, (b) amount of different Pt species, (c) Co 2p, (d) amount of different Co species, and (e) Ce 3d XPS spectra of samples. (f) Schematic illustrations of reaction pathways for hydrogenation of ethynylbenzene over ternary PtCoCe RE alloy. Differential charge density of (g) PtCo and (h) PtCoCe slab models. The yellow and blue isosurfaces present electron accumulation and donation, respectively. (i) The Bader charge of atoms from various structures.

remains essentially unchanged (Figure S17). This electronic reconstruction establishes a multistage charge transfer pathway, which correlates with the observed catalytic enhancement. The schematic atomic graph of a representative crystal structure (Figure 4f) illustrates that the ternary PtCoCe alloy catalytic system employs a rare-earth electronic valve effect (manipulated by Ce), which facilitates directional electron transfer through interfacial charge redistribution. Synergistic electronic coupling between Ce, Co and Pt induces a multistage charge redistribution pathway (Ce-Co-Pt), where Ce acts as an electronic modulator enhances interfacial electron transfer, optimizing the electronic configuration of Pt. This not only accelerates H<sub>2</sub> dissociation via electron-rich Pt but also suppresses over-hydrogenation by reducing the binding energy of styrene intermediates, thereby improving selectivity. Subsequent analysis further proved the mechanism.

Density functional theory (DFT) calculations were performed to elucidate the intrinsic mechanism underlying enhanced

ethynylbenzene hydrogenation performance. The representative Pt, PtCo, and PtCoCe slab models were constructed (Figures S18). The charge density difference analysis of PtCo and PtCoCe alloys further revealed the synergistic electronic coupling between Co and Ce, which collectively modulate the electronic configuration of Pt active sites (Figure 4g, h, S19). Specifically, the Bader charges analysis identified a charge transfer from Co to Pt in the PtCo system (Figure 4i), where Pt atoms accumulated -0.30 |e<sup>-</sup>| while adjacent Co atoms exhibited electron depletion (+0.29 |e<sup>-</sup>|). In contrast, the introduction of Ce into the ternary PtCoCe alloy causes a more pronounced charge polarization. Here, Ce acts as the primary electron donor (+1.05 |e<sup>-</sup>|), transferring electrons to both surface Pt (-0.76 |e<sup>-</sup>|) and Co (-0.19 |e<sup>-</sup>|) atoms.

The projected density of states (PDOS) analysis illustrates the pivotal role of Ce in tailoring the electronic structure

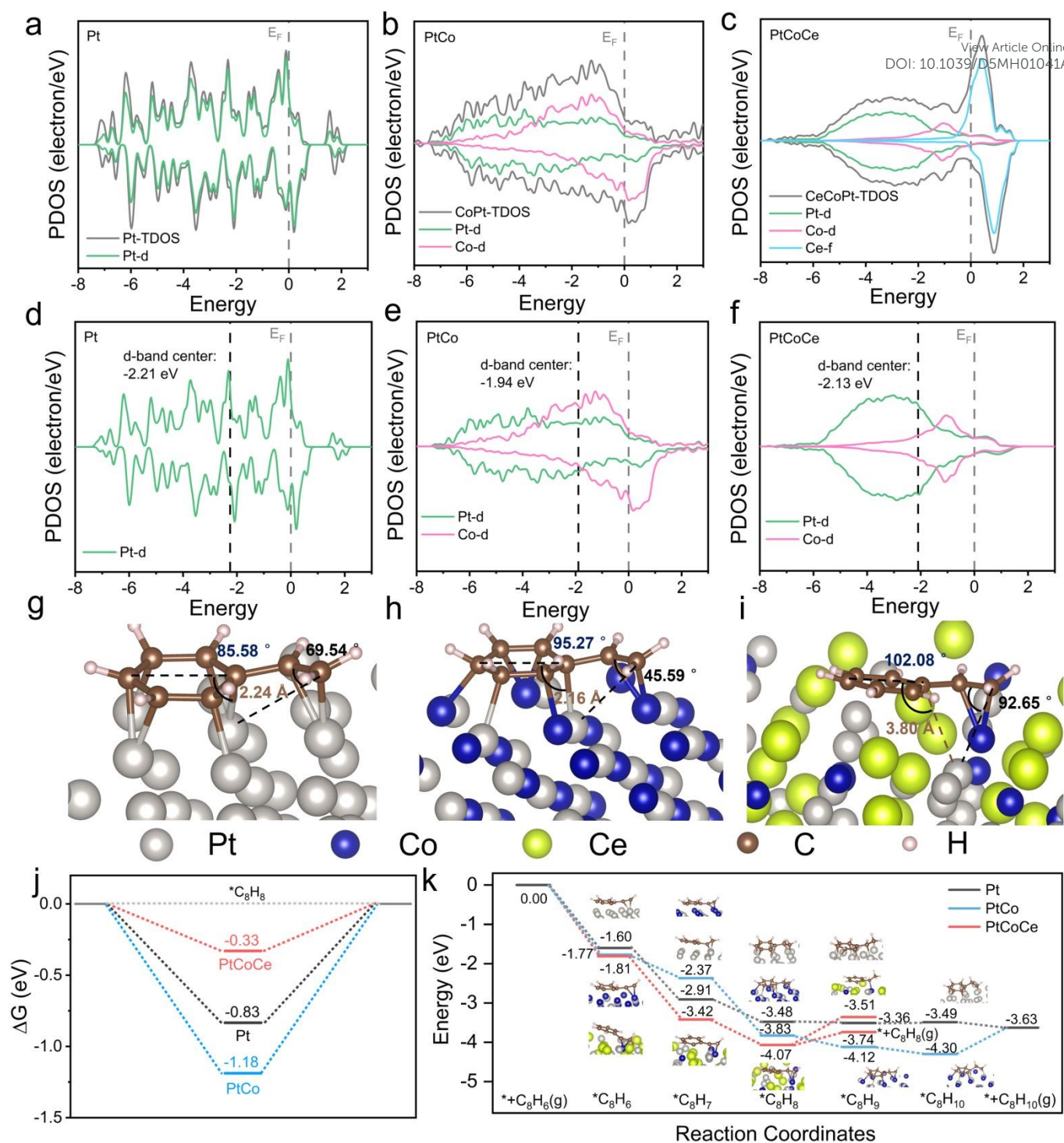


**Figure 5** (a-c) The PDOSs of Pt, PtCo, and PtCoCe. (d-f) The d orbital states of Pt/C, PtCo/C, and PtCoCe/C. (g-i) Adsorption configurations of  $^*C_8H_8$  at interfaces of Pt, PtCo, and PtCoCe models. The light pink, brown, grey, blue and yellow balls represent hydrogen, carbon, platinum, cobalt and cerium atoms, respectively. (j) The Gibbs free energy of styrene adsorption over PtCoCe (red line), PtCo (blue line), and Pt (black line). (k) The reaction energies for the hydrogenation of styrene over PtCoCe, PtCo, and Pt.

across alloy configurations (Figure 5a-c). In the Pt-dominated system (Pt-TDOS), the valence region near the Fermi level ( $E_F$ ) is predominantly governed by Pt-d orbitals. Upon introducing Co, hybridization between Pt-d and Co-d orbitals emerges, signifying the charge redistribution. In the ternary PtCoCe system, Ce-4f orbitals generate a pronounced electron density near  $E_F$ , characterized by sharp, overlapping peaks that enhance interorbital coupling and facilitate efficient electron transfer.

Concurrently, the Pt-d band undergoes substantial broadening, while Co-d orbital split into dual peaks, reflecting synergistic d-f orbital interactions. This f-orbital dominance near  $E_F$  optimizes the d-band center through efficient site-to-site charge transfer between Ce and Pt (Co) atoms. The evolution of the d-band center is quantitatively analyzed by the projected state density (PDOS) of the Pt-d orbitals (Figure

5d-f). The results reveal that PtCoCe has a moderate d-band center position at -2.13 eV, which is neither too distant nor too close to the  $E_F$  compared with PtCo (-1.94 eV) and Pt (-2.21 eV). This suggests that PtCoCe possesses an optimal binding strength for intermediates on the Pt-Co active site and reduces the kinetic barriers for intermediate desorption, thereby enhancing both charge transfer efficiency and reactant adsorption on its surface. These structural modifications underscore Ce's dual role, which act as an electronic modulator to tailor orbital hybridization and as a charge reservoir to redistribute electron density across Pt and Co active sites. The adsorption configurations and desorption dynamics of styrene ( $C_8H_8$ ) on Pt, PtCo, and PtCoCe catalysts were systematically investigated to unravel the geometric and electronic modulation effects on catalytic selectivity. The benzene ring and double bond of styrene exhibited distinct variations in bond lengths and angles upon adsorption on Pt, PtCo, and PtCoCe surfaces (Figures S20 and S21, Tables S7 and S8). On pristine Pt, the phenyl ring adsorbs in a near-parallel orientation ( $\angle C_1-C_6-Pt = 85.58^\circ$ ), characterized by a Pt- $C_6$  bond length of 2.24 Å and a C=C-Pt bond angle of 69.54° (Figure 5g), facilitating strong  $\pi$ -interaction and moderate chemisorption (C=C bond elongation to 1.42 Å).<sup>63</sup> In contrast, PtCo exhibits enhanced metal-substrate interaction, shortening the Pt- $C_6$  bond to 2.16 Å and the C=C bond to 1.41 Å (Figure 5h), but introduces a tilted phenyl ring (95.27°) due to Co-driven electronic effects. Remarkably, the ternary PtCoCe catalyst exhibits a distinct geometric distortion due to Ce doping, which induces significant steric hindrance.<sup>64</sup> This effect forces the phenyl ring into a highly tilted orientation (102.08°) accompanied by a Pt- $C_6$  bond elongation (3.80 Å) and an adjusted C=C-Pt bond angle (92.65°) (Figure 5i). These structural modifications disrupt  $\pi$ -orbital overlap between the aromatic system and the catalyst surface, substantially weakening chemisorption strength. The steric bulk of Ce atoms further destabilizes the adsorbed configuration, lowering the desorption energy barrier to 0.33 eV (vs. 0.83 eV on Pt and 1.18 eV on PtCo). Such geometric modulation not only reduces intermediate over-stabilization but also promotes efficient desorption, thereby aligning with the enhanced catalytic selectivity observed in hydrogenation reactions. The calculated Gibbs free energy ( $\Delta G$ ) reveals a well-tuned binding strength on the geometrically modulated catalyst surface (Figure 5j). Specifically, PtCo exhibits the strongest adsorption affinity for  $C_8H_8$ , with the energy required for  $*C_8H_8$  desorption in the order of PtCo (1.18 eV) > Pt (0.83 eV) > PtCoCe (0.33 eV). This trend indicates that the PtCoCe catalyst facilitates significantly easier desorption of intermediates compared to Pt and PtCo. The lower desorption energy barrier on PtCoCe minimizes intermediate accumulation on the catalyst surface, thereby mitigating surface poisoning and enhancing the overall catalytic cycle efficiency. The Gibbs adsorption free energy ( $\Delta G$ ) of ethynylbenzene semi-hydrogenation on Pt, PtCo, and PtCoCe catalysts were calculated to elucidate the hydrogenation mechanism from energetic perspective. The adsorption energies and energy barriers for all key steps in the hydrogenation process, as well as the corresponding configurations of the intermediates involved, are provided in Figures 5k, S22, and Table S9. The results show that the

adsorption energies on PtCoCe for  $C_8H_6$  is -1.81 eV, significantly higher than those of Pt (-1.60 eV) and PtCo (-1.77 eV). For the hydrogenation of  $C_8H_6$  to  $C_8H_8$ , the stepwise free energy profiles for all three catalysts present a downward trend, indicating that the thermodynamically spontaneous reaction pathways. The total free energies for this conversion process are -1.88 eV (Pt), -2.06 eV (PtCo), and -2.26 eV (PtCoCe), among PtCoCe exhibits the largest energy reduction, revealing more thermodynamically favorable pathway for  $C_8H_8$  formation relative to Pt and PtCo. In addition, the energy barrier for hydrogenating  $*C_8H_8$  to  $*C_8H_9$  on PtCoCe is 0.70 eV, while the desorption energy of  $*C_8H_8$  is only 0.33 eV. Since the desorption energy is significantly lower than the hydrogenation barrier,  $*C_8H_8$  preferentially desorbs from PtCoCe rather than undergoing further hydrogenation. In contrast, the hydrogenation step on PtCo is thermodynamically favorable ( $\Delta G = -0.29$  eV), whereas desorption requires a higher energy (+1.18 eV), forcing the adsorbed  $*C_8H_8$  toward hydrogenation. The subsequent conversion is highly exothermic ( $\Delta G = -0.18$  eV), which demonstrates that the styrene is prone to be hydrogenated to the undesired ethylbenzene. Similar results are also seen on the Pt, on which the free energy barrier for the hydrogenation of  $*C_8H_8$  ( $\Delta G = -0.03$  eV) is much lower than the desorption free energy (+0.83 eV), favoring hydrogenation over desorption. The final step exhibits a near-neutral free energy change ( $\Delta G = +0.01$  eV) and slower kinetics compared to PtCo. Rare earth doping introduces steric hindrance to destabilize alkyne adsorption geometries and enhance olefin desorption kinetics, effectively decoupling activity-selectivity limitations by mitigating site blocking and suppressing over-hydrogenation. These findings underscore the critical role of rare earth elements in tailoring adsorption geometries through steric effects, offering a strategic avenue to optimize catalyst performance by balancing activation and desorption dynamics.

## Conclusions

In summary, a series of ternary  $Pt_{2-x}Co_xCe$  rare earth alloy catalysts have been rationally designed that achieve electronic-geometric synergy, enabling simultaneous optimization of ethynylbenzene activation and styrene selectivity. Comprehensive characterization reveals that directional electron transfer from Ce (4f) to Pt/Co (5d) orbitals via d-f orbital hybridization regulate the Pt d-band center to -2.138 eV, precisely balancing C≡C bond dissociation and intermediate styrene desorption; Moreover, steric distortion arising from the large ionic radius of rare earth tilts styrene's adsorption geometry, which reduces adsorption energy while elevating the over-hydrogenation energy barrier. The synergistic interplay between electronic optimization of active sites and geometric confinement of intermediates preserves rapid ethynylbenzene conversion while kinetically suppressing ethylbenzene formation. The detailed performance studies revealed that the optimal  $Pt_{1.5}Co_{0.5}Ce/C$  catalyst delivers 98.3%

conversion, 85.1% selectivity, and a TOF of 1549.6 h<sup>-1</sup> under mild conditions, surpassing the most previously reported Pt-based catalysts. This study repositions rare earth elements as active modulators of electronic/geometric in catalysis, overcoming classical limitations in industrial hydrogenation and paving the way for sustainable chemical synthesis.

## Author contributions

Investigation, K. J.; data curation, K. J.; writing - original draft, K. J.; writing - review & editing, K. J., J. Y., L. Z., and Y. D.; formal analysis, K. J., W. Z., H. L., J. S., S. W., Z. Z., and Y. D.; funding acquisition, Y. D. All authors discussed the results and the manuscript. All authors have agreed to the published version of the manuscript.

## Conflicts of interest

There are no conflicts to declare.

## Data availability

The data underlying this study are available in the published article and its online ESI.†

## Acknowledgements

We gratefully acknowledge the support from the Advanced Materials-National Science and Technology Major Project, No. 2024ZD0606500, National Science Foundation for Distinguished Young Scholars of China (22425503), National Natural Science Foundation of China (22371131), the 111 Project (B18030) from China, and the Key Laboratory of Rare Earths, Chinese Academy of Sciences.

## References

- D. Teschner, J. Borsodi, A. Wootsch, Z. Revay, M. Hävecker, A. Knop-Gericke, S. D. Jackson, R. Schlögl, *Science* 2008, **320**, 86.
- J. T. Kleinhaus, J. Wolf, K. Pellumbi, L. Wickert, S. C. Viswanathan, K. J. Puring, D. Siegmund, U. Apfel, *Chem. Soc. Rev.*, 2023, **52**, 7305.
- R. Qin, L. Zhou, P. Liu, Y. Gong, K. Liu, C. Xu, Y. Zhao, L. Gu, G. Fu, N. Zheng, *Nat. Catal.*, 2020, **3**, 703.
- L. Jiang, K. Liu, S.-F. Hung, L. Zhou, R. Qin, Q. Zhang, P. Liu, L. Gu, H. M. Chen, G. Fu, N. Zheng, *Nat. Nanotechnol.*, 2020, **15**, 848.
- J. Bu, Z. Liu, W. Ma, L. Zhang, T. Wang, H. Zhang, Q. Zhang, X. Feng, J. Zhang, *Nat. Catal.*, 2021, **4**, 557.
- M. Crespo-Quesada, F. Cárdenas-Lizana, A. L. Dessimoz, L. Kiwi-Minsker, *ACS Catal.*, 2012, **2**, 1773.
- F. Studt, F. Abild-Pedersen, T. Bligaard, R. Z. Sørensen, C. H. Christensen, J. K. Nørskov, *Science* 2008, **320**, 1320.
- L. M. Zhao, X. T. Qin, X. R. Zhang, X. B. Cai, F. Huang, Z. M. Jia, J. Y. Diao, D. Q. Xiao, Z. Jiang, R. F. Lu, N. Wang, H. Y. Liu, D. Ma, *Adv. Mater.*, 2022, **34**, 2110455.
- L. Shao, X. Huang, D. Teschner, W. Zhang, *ACS Catal.*, 2014, **4**, 2369.
- W. Zhang, K. Uwakwe, J. Hu, Y. Wei, J. Zhu, W. Zhou, C. Ma, L. Yu, R. Huang, D. Deng, *Nat. Commun.*, 2024, **15**, 9457.
- C. Shen, Y. Ji, P. Wang, S. Bai, M. Wang, Y. Li, X. Huang, Q. Shao, *ACS Catal.*, 2021, **11**, 5231.
- Z. Wang, Q. Luo, S. Mao, C. Wang, J. Xiong, Z. Chen, Y. Wang, *Nano Res.*, 2022, **15**, 10044.
- J. Carlos, S. Miquel, D. Agusti, L. Bertran, *J. Am. Chem. Soc.*, 1987, **109**, 7623.
- G. C. Bond, G. Webb, P. B. Wells, J. M. Winterbottom, *J. Catal.*, 1962, **1**, 74.
- Z. S. Wang, A. Garg, L. X. Wang, H. R. He, A. Dasgupta, D. Zanchet, M. J. Janik, R. M. Rioux, Y. Román-Leshkov, *ACS Catal.*, 2020, **10**, 6763.
- Q. Guo, R. T. Chen, J. P. Guo, C. Qin, Z. T. Xiong, H. X. Yan, W. B. Gao, Q. J. Pei, A. A. Wu, P. Chen, *J. Am. Chem. Soc.*, 2021, **143**, 20891.
- L. Shen, S. Mao, J. Li, M. Li, M. P. Chen, H. Li, Z. Chen, Y. Wang, *J. Catal.*, 2017, **350**, 13.
- J. Boitiaux, J. Cosyns, S. Vasudevan, *Appl. Catal.*, 1985, **15**, 317.
- Y. Kuwahara, H. Kango, H. Yamashita, *ACS Catal.*, 2019, **9**, 1993.
- W. Wu, N. Li, C. Che, J. Zhao, J. Qin, Z. Feng, J. Song, Z. Zhang, R. Zhang, Y. Long, *Angew. Chem. Int. Ed.*, 2024, **63**, e202410246.
- L. Xia, D. Li, J. Long, F. Huang, L. Yang, Y. Guo, Z. Jia, J. Xiao, H. g Liu, *Carbon* 2019, **145**, 47.
- G. Vilé, S. Colussi, F. Krumeich, A. Trovarelli, J. Pérez-Ramírez, *Angew. Chem. Int. Ed.*, 2014, **53**, 12069.
- A. Han, J. Zhang, W. Sun, W. Chen, S. Zhang, Y. Han, Q. Feng, L. Zheng, L. Gu, C. Chen, Q. Peng, D. Wang, Y. Li, *Nat Commun.*, 2019, **10**, 3787.
- X. Lin, F. Hu, Q. Li, D. Xu, Y. Xu, Z. Zhang, J. Chen, X. Li, *J. Am. Chem. Soc.*, 2024, **146**, 18451.
- F. Zhang, Y. Zhang, J. Wang, Q. Wang, H. Xu, D. Li, J. Feng, X. Duan, *Angew. Chem. Int. Ed.*, 2024, **63**, e202412637.
- Z. Sun, C. Li, J. Lin, T. Guo, S. Song, Y. Hu, Z. Zhang, W. Yan, Y. Wang, Z. Wei, F. Zhang, K. Zheng, D. Wang, Z. Li, S. Wang, W. Chen, *ACS Nano* 2024, **18**, 13286.
- K. Yan, X. Ge, Y. Cao, Y. Qiang, J. Zhang, S. Dai, G. Qian, D. Chen, X. Zhou, W. Yuan, X. Duan, *Angew. Chem. Int. Ed.*, 2025, e202503263.
- J. Su, Y. Ji, S. Geng, L. Li, D. Liu, H. Yu, B. Song, Y. Li, C. Pao, Z. Hu, X. Huang, J. Lu, Q. Shao, *Adv. Mater.*, 2024, **36**, 2308839.
- L. Meng, C. Kao, Z. Wang, J. Ma, P. Huang, N. Zhao, X. Zheng, M. Peng, Y.-R. Lu, Y. Tan, *Nat Commun.*, 2024, **15**, 5999.
- Y. Jin, P. Wang, X. Mao, S. Liu, L. Li, L. Wang, Q. Shao, Y. Xu, X. Huang, *Angew. Chem. Int. Ed.*, 2021, **60**, 17430.
- X. Yang, C. Xing, B. Zhang, X. Liu, H. Liang, G. Luo, G. Zhang, Z. Li, S. Zhao, J. Zhang, G. Wang, Y. Qin, *ACS Catal.*, 2022, **12**, 10849.
- Z. Dong, C. Zhou, W. Chen, F. Lin, H. Luo, Z. Sun, Q. Huang, R. Zeng, Y. Tan, Z. Xiao, H. Huang, K. Wang, M. Luo, F. Lv, S. Guo, *Adv. Funct. Mater.*, 2024, **34**, 2400809.
- Y. Sun, J. Xie, Z. Fu, H. Zhang, Y. Yao, Y. Zhou, X. Wang, S. Wang, X. Gao, Z. Tang, S. Li, X. Wang, K. Nie, Z. Yang, Y. Yan, *ACS Nano* 2023, **17**, 13974.
- K. Jiang, Y. Jiang, Z. Liang, C. Gu, Z. Shen, Y. Du, *Adv. Funct. Mater.*, 2024, **34**, 2411094.
- S. Ajmal, A. Rasheed, W. Sheng, G. Dastgeer, Q. Nguyen, P. Wang, P. Chen, S. Liu, Q. Viet, M. Zhu, P. Li, D. Wang, *Adv. Mater.*, 2025, **37**, 2412173.
- J. Liu, P. Li, S. Jia, Y. Wang, L. Jing, Z. Liu, J. Zhang, Q. Qian, X. Kang, X. Sun, Q. Zhu, B. Han, *Nat. Synth.*, 2025, **4**, 730.
- K. Jiang, Z. Li, Z. Zhang, J. Li, X. Qi, J. Zhou, X. Wang, H. Wei, H. Chu, *Inorg. Chem.*, 2023, **62**, 8145.
- J. Xia, H. Zhao, B. Huang, L. Xu, M. Luo, J. Wang, F. Luo, Y. Du, C. Yan, *Adv. Funct. Mater.*, 2020, **30**, 1908367.
- M. Li, X. Wang, K. Liu, H. Sun, D. Sun, K. Huang, Y. Tang, W. Xing, H. Li, G. Fu, *Adv. Mater.*, 2023, **35**, 2302462.
- Y. Jiang, Z. Liang, J. Liu, H. Fu, C.-H. Yan, Y. Du, *ACS Nano* 2024, **18**, 19137.
- J. Liu, P. Li, J. Bi, S. Jia, Y. Wang, X. Kang, X. Sun, Q. Zhu, B. Han, *J. Am. Chem. Soc.*, 2023, **145**, 23037.
- R. Cheng, X. He, M. Jiang, X. Shao, W. Tang, B. Ran, H. Li, C. Fu, *Adv. Funct. Mater.*, 2025, 2425138.

- 43 C. Wang, X. Wu, H. Sun, Z. Xu, C. Xu, X. Wang, M. Li, Y. Wang, Y. Tang, J. Jiang, K. Sun, G. Fu, *Energy Environ. Sci.*, 2025, **18**, 4276.
- 44 M. Escudero-Escribano, P. Malacrida, M. H. Hansen, U. G. Vej Hansen, A. Velazquez-Palenzuela, V. Tripkovic, J. Schiötz, J. Rossmeisl, I. E. L. Stephens, I. Chorkendorff, *Science* 2016, **352**, 73.
- 45 Y. Hu, J. Jensen, L. Cleemann, B. Brandes, Q. Li, *J. Am. Chem. Soc.*, 2020, **142**, 953.
- 46 Y. Hu, J. Jensen, P. Norby, L. Cleemann, F. Yang, Q. Li, *Chem. Mater.*, 2021, **33**, 535.
- 47 T. Moriyama, S. Muratsugu, M. Sato, K. Higuchi, Y. Takagi, M. Tada, *J. Am. Chem. Soc.*, 2025, **147**, 1262.
- 48 Z. Wu, Y. Liu, D. Wang, Y. Zhang, K. Gu, Z. He, L. Liu, H. Liu, J. Fan, C. Chen, S. Wang, *Adv. Mater.*, 2024, **14**, 2309470.
- 49 M. Xie, Z. Lyu, R. Chen, M. Shen, Z. Cao, Y. Xia, *J. Am. Chem. Soc.*, 2021, **143**, 8509.
- 50 Z. Li, F. Meng, X. Yang, Y. Qi, Y. Qin, B. Zhang, *ACS Catal.*, 2024, **14**, 5016.
- 51 P. Deng, J. Duan, F. Liu, N. Yang, H. Ge, J. Gao, H. Qi, D. Feng, M. Yang, Y. Qin, Y. Ren, *Angew. Chem. Int. Ed.*, 2023, **62**, e202307853.
- 52 K. Yan, X. Ge, Y. Cao, Y. Qiang, J. Zhang, S. Dai, G. Qian, D. Chen, X. Zhou, W. Yuan, X. Duan, *Angew. Chem. Int. Ed.*, 2025, e202503263
- 53 Q. Luo, H. Wang, Q. Xiang, Y. Lv, J. Yang, L. Song, X. Cao, L. Wang, F. Xiao, *J. Am. Chem. Soc.*, 2024, **146**, 26379.
- 54 H. Wu, X. Yang, S. Zhao, L. Zhai, G. Wang, B. Zhang, Y. Qin, *Chem. Commun.*, 2022, **58**, 1191.
- 55 D. Gao, S. Wang, Y. Lv, C. Wang, J. Ren, P. Zheng, L. Song, A. Duan, X. Wang, G. Chen, C. Xu, *ACS Catal.*, 2024, **14**, 1939.
- 56 X. Ge, Y. Jing, N. Fei, K. Yan, Y. Liang, Y. Cao, J. Zhang, G. Qian, L. Li, H. Jiang, X. Zhou, W. Yuan, X. Duan, *Angew. Chem. Int. Ed.*, 2024, **63**, e202410979.
- 57 S. Ji, C. Zhang, R. Guo, Y. Jiang, T. He, Q. Zhan, R. Li, Y. Zheng, Y. Li, S. Dai, X. Yang, M. Jin, *ACS Catal.*, 2024, **14**, 11721.
- 58 H. Cai, H. Yang, S. He, D. Wan, Y. Kong, D. Li, X. Jiang, X. Zhang, Q. Hu, C. He, *Angew. Chem. Int. Ed.*, 2025, **64**, e202423765.
- 59 M. Li, X. Wang, K. Liu, Z. Zhu, H. Guo, M. Li, H. Du, D. Sun, H. Li, K. Huang, Y. Tang, G. Fu, *Adv. Energy Mater.*, 2023, **13**, 2301162.
- 60 L. Zhai, X. She, L. Zhuang, Y. Li, R. Ding, X. Guo, Y. Zhang, Y. Zhu, K. Xu, H. J. Fan, S. Lau, *Angew. Chem. Int. Ed.*, 2022, **61**, e202116057.
- 61 C. Duan, J. Liu, Z. Li, R. Shi, J. Zhao, G. I. N. Waterhouse, X. Wen, L. Zhang, L. Wu, T. Zhang, *Adv. Mater.*, 2025, **37**, 2411648.
- 62 S. Zhang, Z. Zeng, Q. Li, B. Huang, X. Zhang, Y. Du, C.-H. Yan, *Energy Environ. Sci.*, 2021, **14**, 5911.
- 63 J. Yang, Y. Sun, H. Shi, H. Zou, Y. Zhang, X. Tian, H. Yang, *J. Am. Chem. Soc.*, 2025, **147**, 5984.
- 64 J. Li, Z. Wang, C. McCallum, Y. Xu, F. Li, Y. Wang, C. M. Gabardo, C. Dinh, T. Zhuang, L. Wang, J. Y. Howe, Y. Ren, E. H. Sargent, D. Sinton, *Nat. Catal.*, 2019, **2**, 1124.

View Article Online  
DOI: 10.1039/D5MH01041A